



ELSEVIER

Contents lists available at ScienceDirect

Planetary and Space Science

journal homepage: www.elsevier.com/locate/pss

Short communication

Rock size-frequency distribution analysis at the Chang'E-3 landing site

Kaichang Di^a, Bin Xu^a, Man Peng^{a,*}, Zongyu Yue^a, Zhaoqin Liu^a, Wenhui Wan^a, Lichun Li^b, Jianliang Zhou^b^a State Key Laboratory of Remote Sensing Science, Institute of Remote Sensing and Digital Earth (RAD), Chinese Academy of Sciences, Beijing 100101, China^b Beijing Aerospace Control Center (BACC), Beijing 100094, China

ARTICLE INFO

Article history:

Received 29 June 2015

Received in revised form

10 November 2015

Accepted 24 November 2015

Available online 18 December 2015

Keywords:

Chang'E-3

Rock size-frequency distribution

Lunar landing sites

ABSTRACT

This paper presents a comprehensive analysis of the rock size-frequency distribution at the Chang'E-3 landing site. Using 84 Navcam stereo images acquired at 7 waypoints by the Yutu rover and an interactive stereo image processing system, a total of 582 rocks larger than 0.05 m in diameter were identified and measured. The statistical results of the size-frequency distribution show that the cumulative fractional area covered by rocks versus their diameter follows a simple exponential function and has a convex-up shape on log–log graphs with the slope increasing with diameter. The cumulative number of rocks versus diameter derived by numerically integrating the cumulative fractional area also shows a good fit with the data. A diameter–height relationship was also determined from height and diameter ratios. The observed rock statistics were also compared with those from other lunar missions, including the Surveyor, Apollo, and Lunokhod missions; results suggest that the rock distribution at the Chang'E-3 landing site is similar to that found by Surveyor III.

© 2015 Elsevier Ltd. All rights reserved.

1. Introduction

Rock populations on the surface of a planet can provide important geological information related to the planet's origin, the evolution of its crust, and the timing of critical events such as volcanism and meteorite bombardment (Garvin et al., 1981; Grant et al., 2006; Ouyang, 2005; Ward et al., 2005; Yingst et al., 2007). Analyzing and characterizing size-frequency distributions of rocks at planetary landing sites is important for understanding the geological history of the region and is also critical in identifying potential hazards in support of future landings and rover navigation (Golombek et al., 2003, 2008; Golombek and Rapp, 1997).

Rock abundance and distribution research has been performed widely on Mars and on the Moon; this research is mostly related to the landing sites of landers and/or rovers. To select suitable landing sites for multiple Mars missions, the detection and characterization of rocks and the relationships of rock size-frequency were usually studied in detail in advance from orbital and ground data (Golombek et al., 2012a). For example, during the Mars Pathfinder (MPF) project's development, the size-frequency distributions of rocks at the two Viking landing sites and Earth analog sites were combined to predict the probability of boulders that were potentially hazardous to the MPF. The results from Viking

Lander 1 and Viking Lander 2 stereo measurements were fitted with exponential functions to model the rock distributions. In addition, the rock size-frequency distributions at Earth analog sites were found to be consistent with those of the two Viking landing sites (Golombek and Rapp, 1997; Golombek et al., 1997). These results were valuable in achieving a safe landing of the Mars Pathfinder lander. The rock distributions from ground observations after the MPF landing fit well with the exponential function and were consistent with prior analyses (Golombek et al., 1999). During Mars Exploration Rover (MER) landing site selection, rock distribution statistics and models were determined from the Imager for the Mars Pathfinder stereo images. Mars Orbiter Camera (MOC) images of 4 MER candidate landing sites (Meridiani Planum, the Gusev crater, Melas Chasma, and Isidis Planitia) were also used to search for boulder fields. The results were used to test the rock distribution model. Furthermore, the cumulative number of rocks per square meter and the probability of impacting rocks larger than 1 m in diameter (Golombek et al., 2003) were estimated using rock abundance estimates from the Viking Infrared Thermal Mapper at the Meridiani and Gusev landing sites (Christensen, 1986). Based on these results, the probability of impacting potentially hazardous rocks at MER landing sites was calculated using an exponential model (Golombek et al., 2003). In addition, with orbital and Spirit rover data, Golombek et al. (2006) provided an overview of the geology of the Gusev cratered plains, over which the rock abundance and maximum block size measured on the ejecta blanket were consistent with expectations.

* Corresponding author. Tel./fax: +86 10 64807987.

E-mail address: pengman@radi.ac.cn (M. Peng).

During the Phoenix landing site selection, Golombek et al. (2008) developed an automated rock-detection algorithm that fit ellipses of shadows and cylinders to rocks. They measured the diameters and heights of ~ 10 million rocks using High Resolution Imaging Science Experiment (HiRISE) images over > 1500 km² of the northern plains. The rock distributions counted in the HiRISE images were also compared with distributions measured from lander images. The size-frequency distributions were extrapolated along model curves to estimate the number of smaller-diameter rocks that could be hazardous to the Phoenix lander (Golombek et al., 2008). The probability of encountering rocks during different phases was also estimated. The estimation proved to match the dearth of large rocks found at the landing site (Heet et al., 2009).

During the Mars Science Laboratory (MSL) mission, Golombek et al. (2012a, 2012b) improved the rock detection techniques which had been used for the Phoenix landing site selection and analyzed rock abundances and size-frequency distributions for the four final sites (Eberswalde crater, the Gale crater, the Holden crater, and Mawrth Vallis) using HiRISE images. The rock abundance at the landing sites was determined by fitting the cumulative number of rocks between 1.5–2.25 m in diameter in 150-m and 450-m bins to the cumulative fractional area distribution. The fitted model predicts that all of the sites were safe with respect to rocks.

Most studies of rock distributions on the Moon have been conducted with data returned by spacecraft that landed there, particularly by the Surveyor series of landers (Shoemaker and Morris, 1968). The Surveyor, Apollo, and Luna programs provided a great deal of detailed information regarding the distributions, compositions, and physical properties of the lunar regolith/rocks at a limited number of sites (Heiken et al., 1991). Shoemaker and Morris (1968) used a power law function to analyze the rock size-frequency distributions at the Surveyor landing sites. The results suggested that fragments larger than 0.1 m occurred more at the Surveyor VII landing site than the Surveyor III, V, and VI landing sites. Mission documents from the six Apollo lunar missions also characterized the geological properties of the landing sites. During the Apollo 11 mission, the cumulative size-frequency distribution of rock fragments larger than 0.32 m was measured from panorama images in the vicinity of the lunar module (LM) (Aldrin et al., 1969). The results suggested that rocks larger than 0.32 m in diameter were more abundant than at the Surveyor landing sites (Aldrin et al., 1969). At the Apollo 16 landing site, the rock size distribution was investigated using panoramic images composed of photographs taken by astronauts. The differential distribution plots of blocks and the cumulative size-frequency indicated that rocks less than 0.1 m in size were the most abundant at stations 5, 6, and, likely, 4. The number of blocks at all stations was inversely proportional to size (Muehlberger et al., 1972). As much as 2.3% of the traversed area was littered with blocks in the 0.1- to 1.0-m size range as well as with smaller blocks that reached the resolution limit (4 cm) (Muehlberger et al., 1972). Recently, Demidov and Basilevsky (2014) studied the height-to-diameter ratios of lunar rocks using 91 panoramic photographs taken by Lunokhod-1, 2, and 17 along with six Lunar Reconnaissance Orbiter Camera (LROC) Narrow Angle Camera (NAC) images. The height-to-visible-diameter and height-to-maximum-diameter ratios were measured for lunar rocks at three highland and mare sites on the Moon. Basilevsky et al. (2015) compared and assessed the results of measurements and observations by the Lunokhod 1 and Yutu rovers; results show that rock shape and degree of preservation of the observed rock fragments in Lunokhod 1 and Chang'E-3 (CE-3) landing sites are rather similar.

Orbital photography images were also used to measure block dimensions and distributions (Cameron and Coyle, 1971; Cintala and McBride, 1994; Moore, 1971). Block distributions in the vicinities of the Surveyor I, III, VI, and VII sites were determined using

Lunar Orbiter photography from the 4 landing sites where spacecraft had recorded data. In addition, orbiter-observed thermal inertia data from the Lunar Reconnaissance Orbiter (LRO) Diviner Radiometer and a lunar thermal model were employed to study rock abundance over a majority of the lunar surface (Bandfield et al., 2011; Bauch et al., 2013; Urquhart and Mellon, 2007). Recently, Qiao et al. (2014) systematically studied the topographic, compositional, stratigraphic, and geological features in Sinus Iridum using multi-source data, i.e., the Lunar Reconnaissance Orbiter Altimeter (LOLA) and Camera (LROC), SELENE Terrain Camera (TC), Clementine ultraviolet-visible (UVVIS), and Chandrayaan-1 Moon Mineralogy Mapper (M3) data. To understand the distributions of blocky ejecta, Bart and Melosh (2007, 2010a, 2010b) investigated the spatial distributions of boulders ejected from lunar impact craters. The results contributed to understanding boulder ejection velocities and the distributions of secondary craters in the Solar System.

The Chinese Lunar Exploration Program (CLEP, also called the Chang'E Program) began in 2004. It includes three phases: orbiting, landing, and returning lunar samples to Earth. Following the successes of the Chang'E-1 (CE-1) and Chang'E-2 (CE-2) orbital missions, the CE-3 mission, which included a lander and a rover, landed successfully at 44.12°N, 19.51°W (radio-tracking solution) on Mare Imbrium of the Moon on December 14, 2013 (Xiao, 2014). The CE-3 lunar rover was the first soft-landing on the Moon since 1976. The stereo images from the rover camera made rock size-frequency analysis possible at the landing site; however, as far as we know, to date no such analysis has been reported.

In this paper, we study the detection and characterization of rocks and the rock size-frequency distributions at the CE-3 landing site, and we perform a detailed comparison with results from other lunar missions. First, the image data and method for rock size measurement from the Yutu rover are described. Next, rock statistics and size-frequency distributions are analyzed and characterized. Finally, the rock distributions from the Yutu rover data are compared with the rock population results from other lunar missions.

2. Study area and data

2.1. The study area: the CE-3 landing site

As the first Chinese lunar soft-lander and rover, the landing site of CE-3 was selected primarily based on engineering constraints including topography, communication, and solar illumination (Zhao et al., 2014). In addition, local geological diversity was taken into consideration, including impact craters, wrinkle ridges, and basaltic materials of various ages (Zhao et al., 2014). Detailed topography mapping of the landing site was conducted before and after the mission by several research/operation teams. For example, Li et al. (2014) generated digital elevation model (DEM) and a digital orthophoto map (DOM) products with different resolutions using CE-2 orbital images and analyzed the geomorphology surrounding the landing site. Based on a DEM generated from Terrain Camera (TC) images of SELENE-1, the topography was found to be relatively flat, with an elevation difference of less than 300 m (Zhao et al., 2014). Wu et al. (2014) characterized the slopes and crater distribution at the CE-3 landing site based on multi-source lunar remote sensing data. They found that the candidate landing area was relatively flat, with a slope of less than 15°. Liu et al. (2015) presented a method for high-precision topographic mapping with multi-source data. Analysis of the geomorphology surrounding the CE-3 landing site shows that the landing area and its surroundings are typical lunar mare with flat topography (Li et al., 2014).

Fig. 1 shows the DEM and DOM of the landing region, which were generated from 80 descent images taken between 217 m and

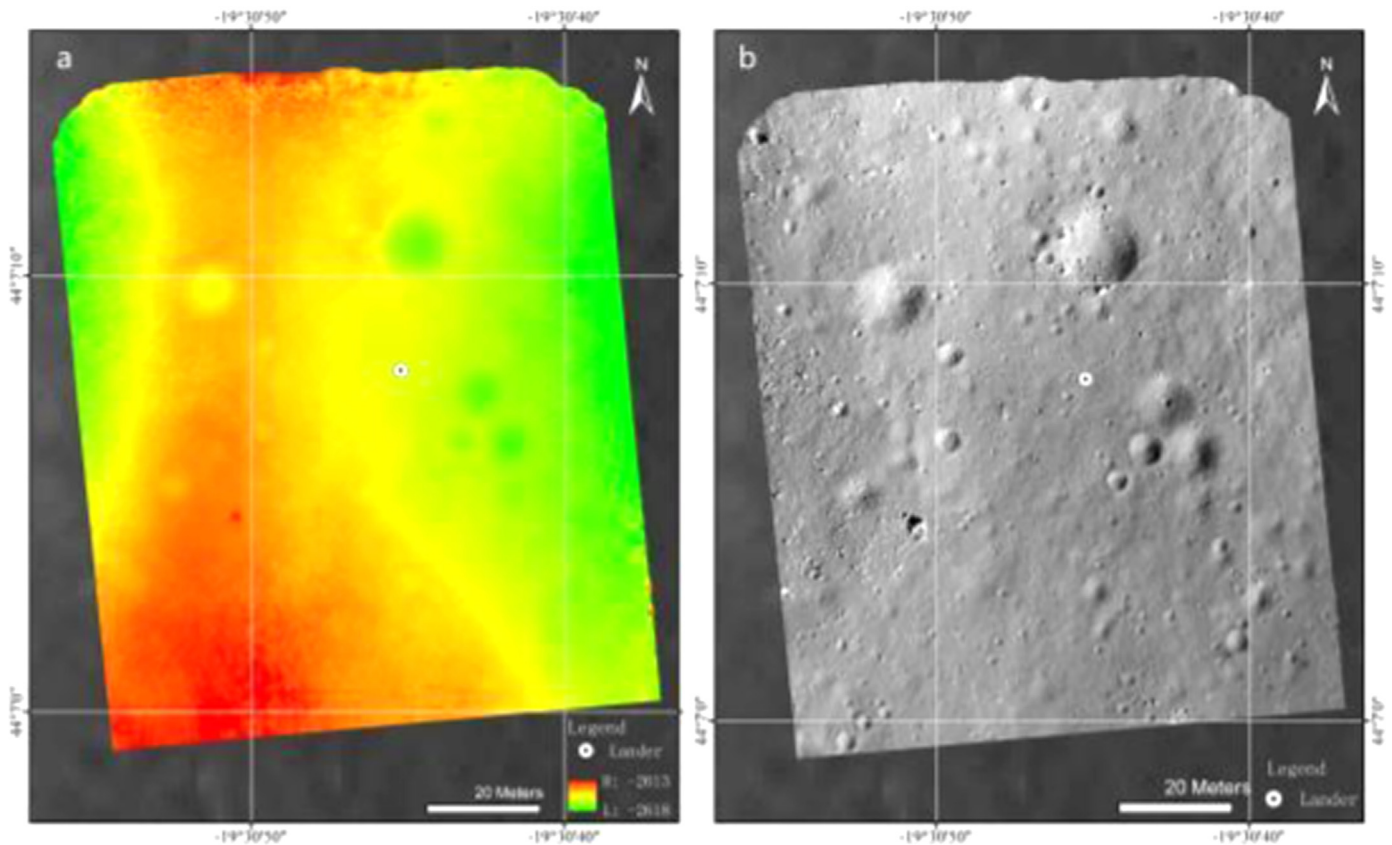


Fig. 1. DEM and DOM of CE-3 landing region. (a) The DEM generated with 0.05-m resolution, covering an area of $97 \text{ m} \times 115 \text{ m}$ with an elevation from $-2,618 \text{ m}$ to $-2,613 \text{ m}$. (b) The DOM generated with a resolution of 0.05 m.

10 m in altitude from the surface with a resolution from 0.168 m/pixel to 0.008 m/pixel (Liu et al., 2015). The white dots in the maps represent the lander position. The lander position is near the borders of two basalt strata and is in the Eratosthenian basalt stratum (Bugiolacchi and Guest, 2008). The maximum local relief is several meters. The northern part of the landing area is in an area with basalt stratum in Mare Imbrium (Wilhelms and McCauley, 1971). The landing site is a high-titanium basalt stratum, and its geological age is young Eratosthenian (Li et al., 2014).

As shown in Fig. 2, the landing site is close to the eastern edge of crater C1 with a diameter of 450 m (Xiao et al., 2015) and was 40 m east of the edge of the crater. There exist many small fresh impact craters on the continuous ejecta deposits of the C1 crater. Fig. 3 shows the traverse map and localization results of the rover waypoints using a cross-site visual localization method. Along the traverse, the rover acquired stereo images that covered 120° of the field. This was realized at each waypoint by using its Navcam in the forward direction with a segment length of approximately 10 m. The base DOM in Fig. 3 was generated from descent images as shown in Fig. 1b. All the waypoints were located on the ejecta blanket of the C1 crater. There is an abundance of subdued craters as large as 3 m in diameter in this region. Most have slightly raised, round rims. Some small craters such as C2 and C3 have excavated boulders larger than $\sim 1 \text{ m}$ in diameter, while smaller nearby craters such as C4 did not penetrate through the surface regolith because no excavated boulders are visible on the crater rims (Xiao et al., 2015).

2.2. CE-3 site data

In this study, Navcam stereo images were used for identifying rocks and measuring rock sizes. The Navcams were mounted on a

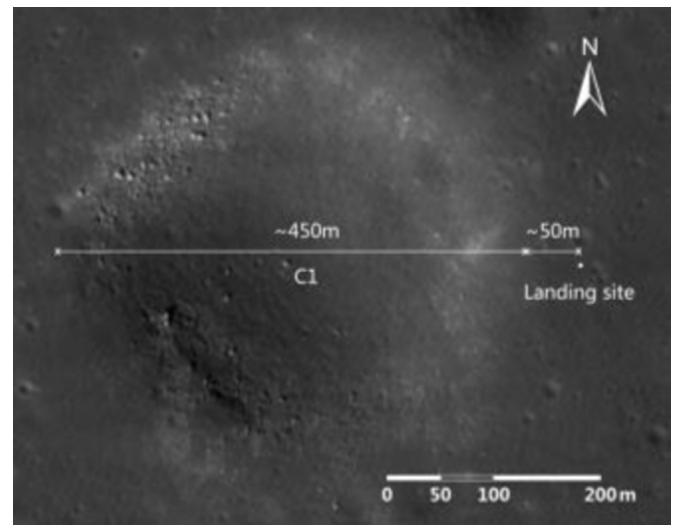


Fig. 2. Yutu landed on the eastern rim of the C1 crater (Xiao et al., 2015).

camera mast 1.5 m above the ground with a stereo base of 0.27 m. The image size of the two identical cameras was 1024×1024 pixels with 0.27 mrad per pixel. The focal length of the cameras was 17.7 mm with a field of view of $46.4^\circ \times 46.4^\circ$. Along the rover traverse, the Navcams usually captured 7 pairs of stereo images at each waypoint. After departing the lander, the Yutu rover traversed 17 waypoints. It acquired 120° -field-of-view forward direction stereo images at 14 waypoints. Stereo images with high resolution and proper lighting conditions were utilized to identify and measure rocks. As a result, stereo pairs from 7 consecutive

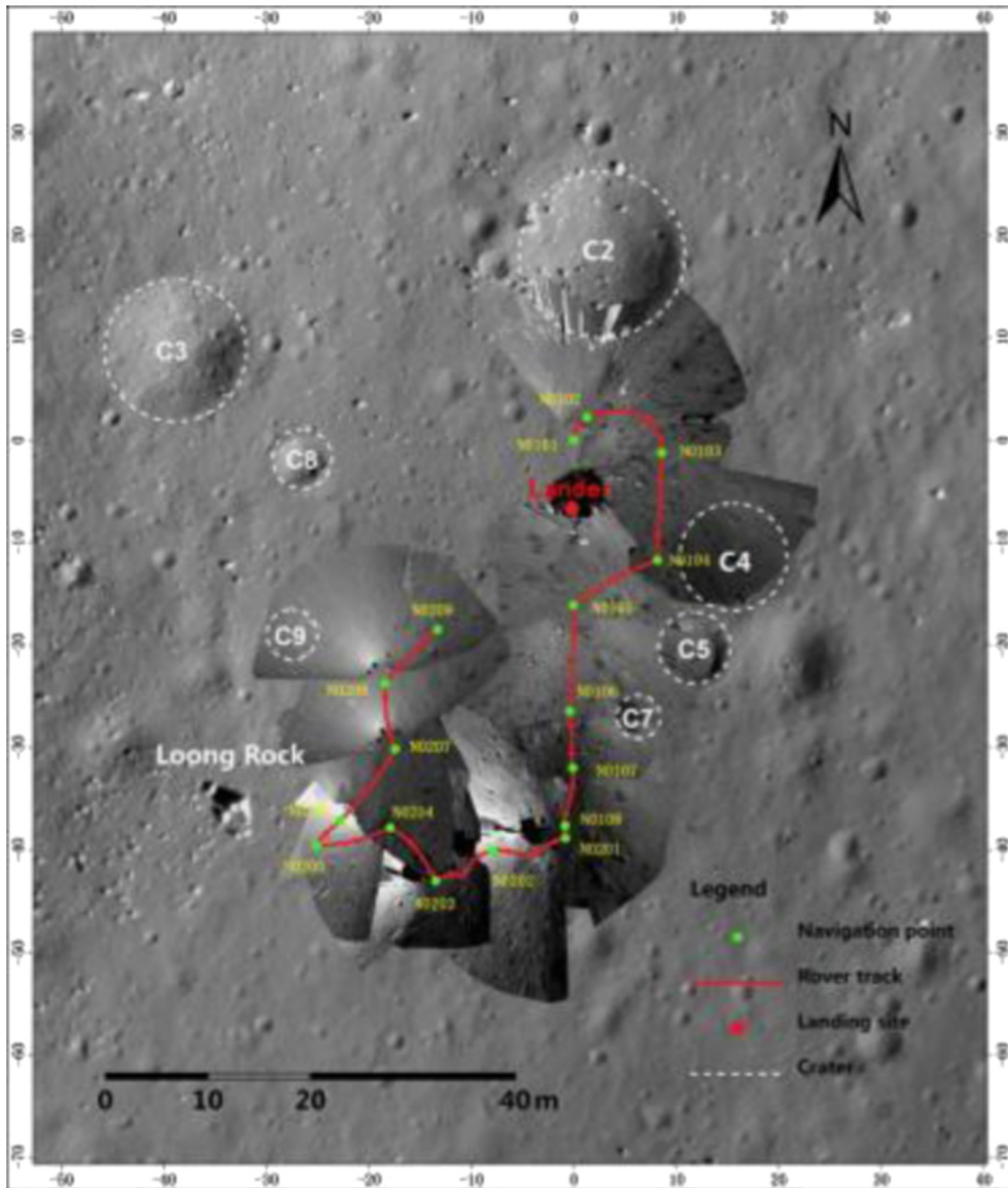


Fig. 3. Traverse map of the CE-3 rover. The overlaid maps are DOMs generated from Navcam stereo images with 0.02-m resolution. The red line shows the rover track, and green points represent waypoints. The crater labels are from [Xiao et al. \(2015\)](#). (For interpretation of the references to color in this figure legend, the reader is referred to the web version of this article.)

Table 1
Details of images used in the project.

Waypoint ID	Location (m)	Start solar azimuth (°)	End solar azimuth (°)
N0101	(0, 0, 0)	30.603	30.627
N0102	(1.27, 2.2, 0.01)	32.209	32.233
N0103	(8.57, -1.25, -0.50)	44.696	44.685
N0104	(8.18, -11.74, -0.5)	43.927	43.914
N0105	(-0.05, -16.12, -0.05)	39.639	39.621
N0106	(-0.40, -26.46, -0.02)	N/A	N/A
N0107	(-0.09, -31.99, 0.02)	N/A	N/A

sites were selected to estimate rock abundance parameters in the landing area. [Table 1](#) lists the information from selected Navcam images. The start/end solar azimuths were retrieved from the header files of the raw data; unfortunately, there is no solar azimuth data available at stations N0106 and N0107. The DOMs of the 14 sites are shown in [Fig. 3](#). [Fig. 4](#) shows two example images from the left Navcam acquired at N0101 and N0102.

3. Method

The original Navcam images were downlinked from the rover and stored in a Planetary Data System (PDS) format. Stereo image processing and mapping software developed in-house was used to

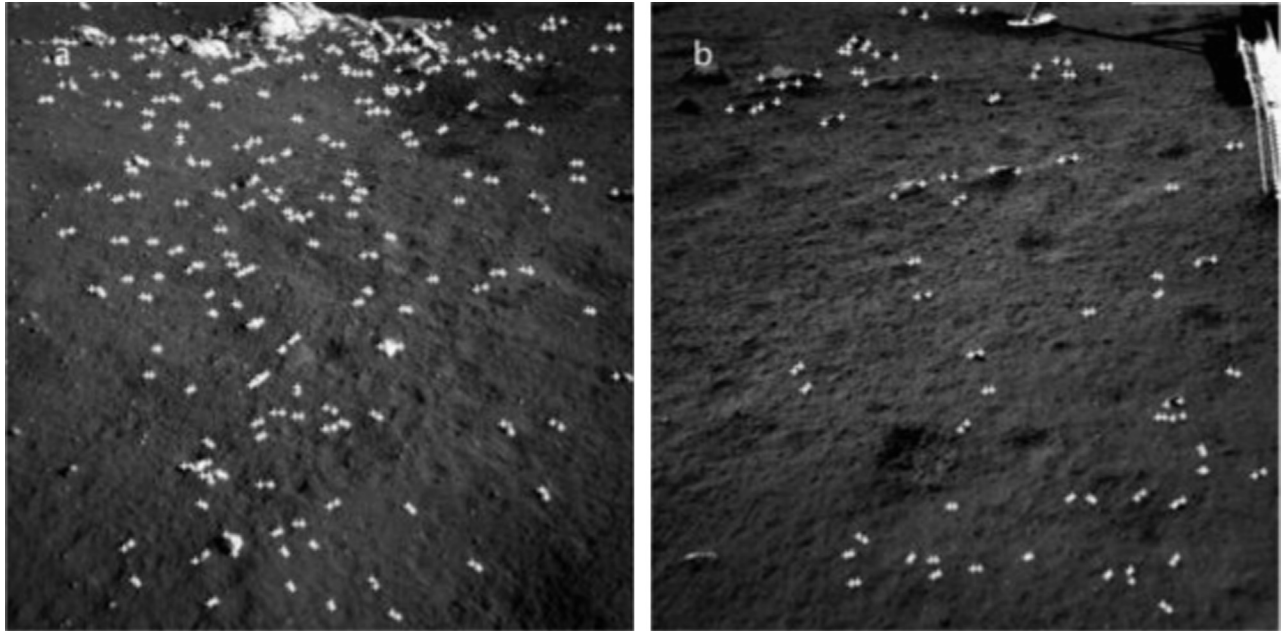


Fig. 4. Examples of Navcam images acquired at waypoints. (a) An image from the left Navcam at site N0101. (b) An image from the left Navcam at site N0102. White crosses are the measured left and right ends of rocks.

process images and measure rocks in 3D. Prior to rock extraction, epipolar images of the Navcam stereo images were generated, and feature point matching was performed on the Navcam images to extract tie points. A bundle adjustment was then applied to the Navcam images at each site to refine their exterior orientation parameters.

After the bundle adjustment, the interactive 3D measurement tool was adapted to measure rocks from the Navcam stereo images. A stereo display mode can be chosen to assist in rock selection and measurement. 3D coordinates can be calculated for any point using the interior and exterior parameters of stereo images. Considering the mapping accuracy of Navcam stereo images and resolution limitations for reliable measurement (Peng et al., 2014), only rocks larger than 0.05 m in object space and greater than 8×8 pixels in image space (regardless of actual size) were considered. Because there are overlapping areas between neighboring sites, duplicate rocks in these areas were counted only once.

When measuring a rock, its endpoints and peak were selected manually on the left image of the stereo pair, and corresponding points were automatically matched on the right image. Consequently, the 3D coordinates of the peaks and endpoints were calculated, and the apparent width W was calculated as the distance between the leftmost and rightmost points. The average rock diameter was then calculated as $0.75W$ (Golombek et al., 2003). In this analysis, the bases of the rocks were assumed to be circular when calculating their areas. Rock height was determined based on the highest and lowest elevation points. All rocks larger than 0.05 m in diameter and taller than 0.001 m were included in the measurement. Fig. 5 shows a typical pair of Navcam images. The white crosses represent the measured ends of rocks, and Fig. 5c and d are the zoomed-in areas of Fig. 5a and b respectively.

4. Results

4.1. Rock statistics

A total of 582 rocks were measured from the Navcam images at the 7 sites (waypoints). Fig. 6 shows the rocks superimposed on

the DOMs. Local concentrations of blocks are found, especially on the east sides and rims of crater C1.

The number of rocks at each site is listed in Table 2. The largest number of rocks was found at site N0101, with 198 rocks.

Fig. 7 shows the histogram of rock diameters for all 7 sites; 61% of rocks are less than 0.1 m in diameter. An exponential function derived through nonlinear least squares fitting is given below and also shown in Fig. 7 as a curve:

$$F = 193.2 \exp(-16.77 \times D) \quad (R^2 = 0.9287) \quad (1)$$

where F represents the number of rocks and D is rock diameter. The curve exhibits a good fit for diameters between 0.07 m and 0.28 m, but it underestimates the number of rocks of smaller and larger diameters.

4.2. Cumulative area results

The model of the cumulative area covered by rocks of a given diameter D or larger can be formulated by an exponential function (Golombek and Rapp, 1997):

$$F_k(D) = k \exp\{-lD\} \quad (2)$$

where k is the total area covered by rocks of all sizes and l is the exponential factor. A least squares method was used to calculate k and l with data from each waypoint and all sites. Table 3 lists the values of all parameters.

The cumulative fractional-area-versus-diameter plot for each waypoint in Fig. 8 shows that the family of curves is not parallel; the portions of the cumulative fractional area distributions at diameters smaller than 0.1 m fit the exponential model better than other portions. The largest area of rocks was found at site N0101, with 8.346 m².

A plot of the cumulative fractional area covered by rocks versus diameter is shown in Fig. 9. The plotted rock data display a convex-up curve shape on log-log graphs. The curve slowly drops off at small diameters, and the slope gradually increases. As shown in Fig. 9, the distribution of rocks fits the exponential model very well for diameters smaller than 1 m.

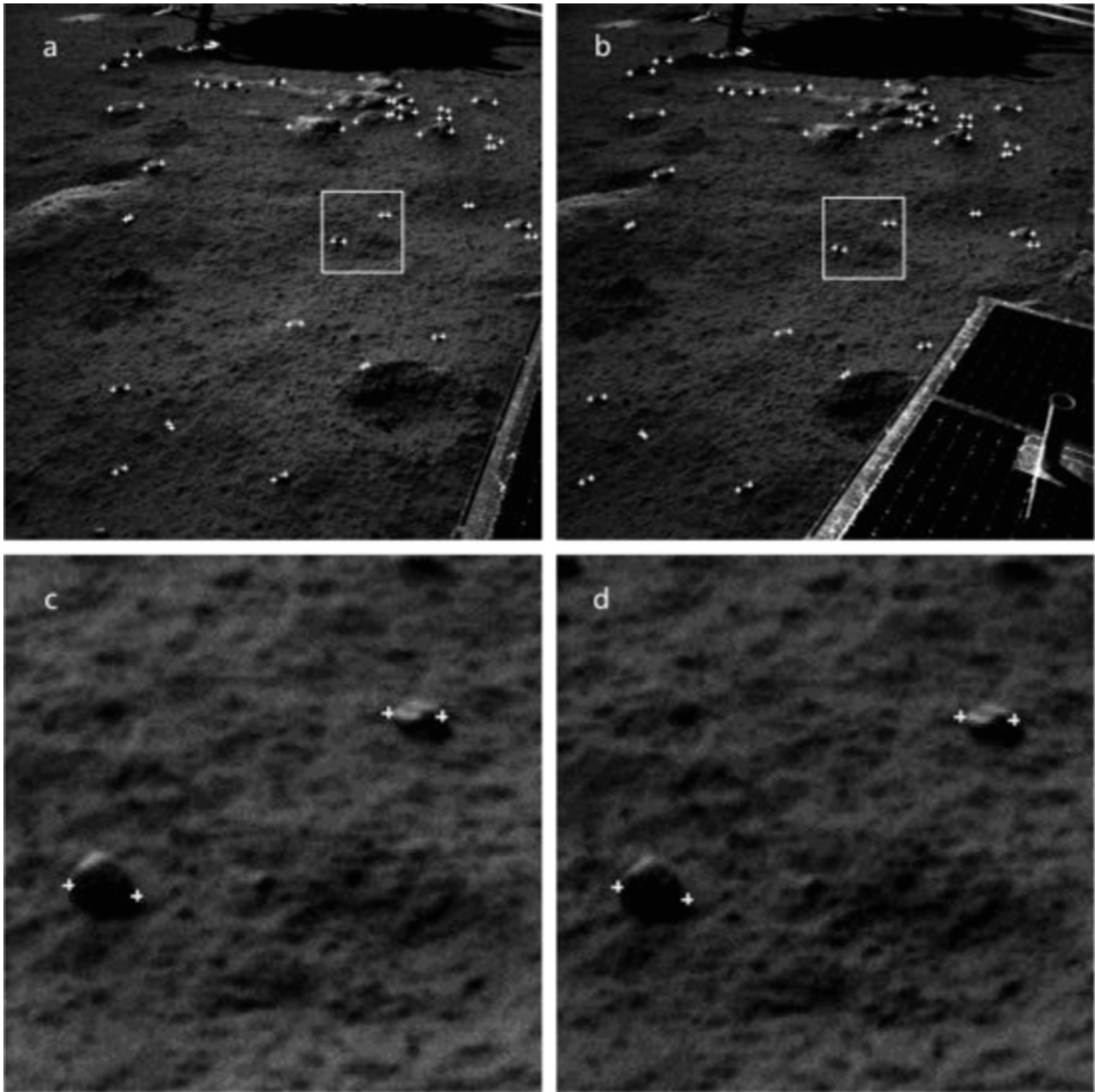


Fig. 5. Rocks measured from Navcam stereo images. (a) The left image, (b) the right image, (c) the enlarged view of the rectangular area in the left image, and (d) the enlarged view of the rectangular area in the right image. White crosses are the measured left and right corners of rocks.

It should be noted that the fitted value of k for the CE-3 site is 0.0125; while various k values have been tried in order to produce the curves in Fig. 9, the range of rock coverage k values in Fig. 9 are 1%, 2%, 3%, and 5% (Golombek and Rapp, 1997). The figure shows that the curve of the whole area was close to the curve when k in Eq. (2) was set to 1%. This means that the areas of the 7 sites occupied by rocks account for nearly 1% of the whole area. In total, an area of 1320.602 m² with medium rock density has a cumulative fractional area distribution that resembles the model curve for 1% rock coverage. Small-diameter rocks account for 1.2% of the total area, while 1-m-diameter boulders account for 0.1%.

4.3. Cumulative number results

The cumulative number of rocks of a given diameter or larger per m² can be modeled with the exponential function below

(Golombek and Rapp, 1997):

$$N(D) = L \exp\{-sD\} \quad (3)$$

where $N(D)$ is the cumulative number of rocks of a given diameter or larger, L represents the total number of rocks of all sizes per square meter, and s is the exponential factor.

However, since inferring cumulative-area-versus-diameter distributions from the cumulative-number-versus-diameter distributions in a mathematically rigorous way introduces a quadratic equation (Golombek and Rapp, 1997), Golombek et al. (2003) derived cumulative-number-versus-diameter distributions by numerically integrating cumulative fractional area curves. For our analysis, we used numerical integration with MATLAB software to derive the cumulative number function. From Eq. (2), it follows that

$$dF = k l e^{ld} dD \quad (4)$$

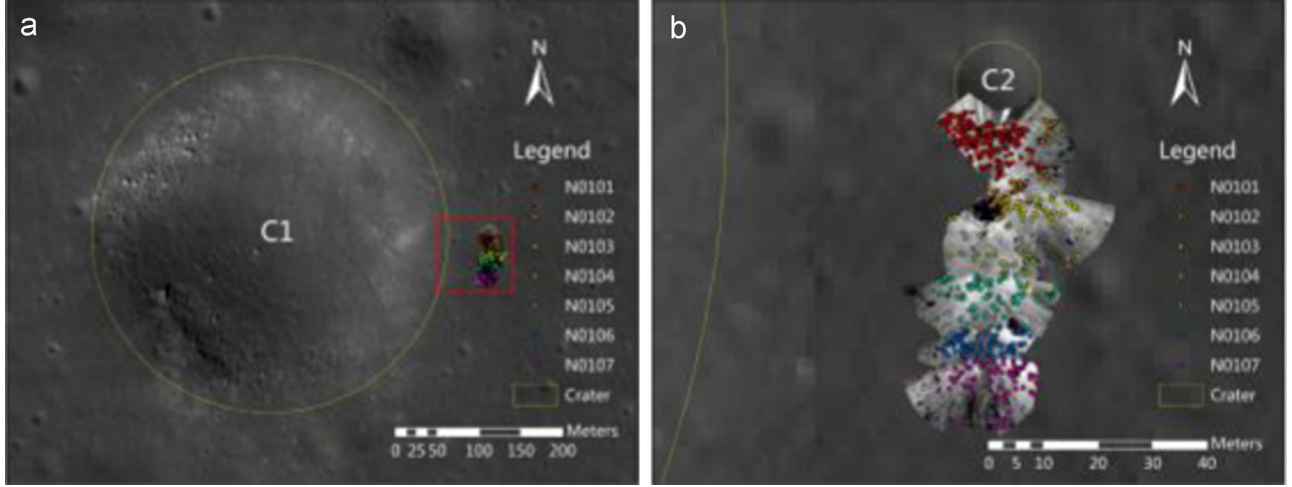


Fig. 6. Rocks superimposed on the DOMs. (a) Seven colors represent rocks extracted from seven sites after removing duplicate rocks; (b) an enlarged view of the rectangular area in (a).

$$dN(D) = \frac{dF}{\pi D^2/4} = \frac{4kl}{\pi} e^{lD} D^{-2} dD \quad (5)$$

where k is 0.0135 and l is -1.734 .

In MATLAB, the integrated function for Eq. (5) can be represented as

$$N(D) = 0.0279 \times \exp(-867/500 \times D)/D - 0.04785 \times Ei(1867/500 \times D) \quad (6)$$

where Ei represents an exponential integral function that can be solved by MATLAB. Finally the cumulative number of rocks of a given diameter or larger can be calculated. As shown in Fig. 10, the cumulative number distributions track the exponential integral function well.

4.4. Generalized diameter–height relationship

A linear relationship was determined between rock height and diameter at the CE-3 landing site. The height of each rock is plotted against its diameter in Fig. 9. The linear least squares fit for the data is given by:

$$H = 0.2347D + 0.0039 \quad (7)$$

In the equation, H represents the height of rocks, indicating that rocks at the site have heights on average $\sim 1/4$ of their diameter. The adjusted R^2 value is 0.8711. Fig. 11 shows that most rocks with heights smaller than 0.1 m and diameters smaller than 0.2 m are concentrated in a small area.

4.5. Comparison with previous mission results

The distributions of rock sizes found at the CE-3 landing site were compared with the distributions observed from the Surveyor, Apollo, and Lunokhod missions. Fig. 12 shows the cumulative number of rocks versus their diameter for the CE-3, Apollo, and Surveyor missions. In general, the number of rocks at all sites is inversely proportional to rock size, with a gradual descent apparent for small rock diameters and a drop off occurring at large diameters. The entire rock distribution curve of the CE-3 site is very close to that of Surveyor I, Surveyor III, and Surveyor VI; in particular, the value is almost equal to that of Surveyor I for rocks with diameters around 0.25 m. Table 4 lists the cumulative number of rocks with diameters larger than 0.1 m. The cumulative number of rocks per square meter for this specific diameter or larger at the CE-3 site (0.17) is close to that for Surveyor VI (0.20).

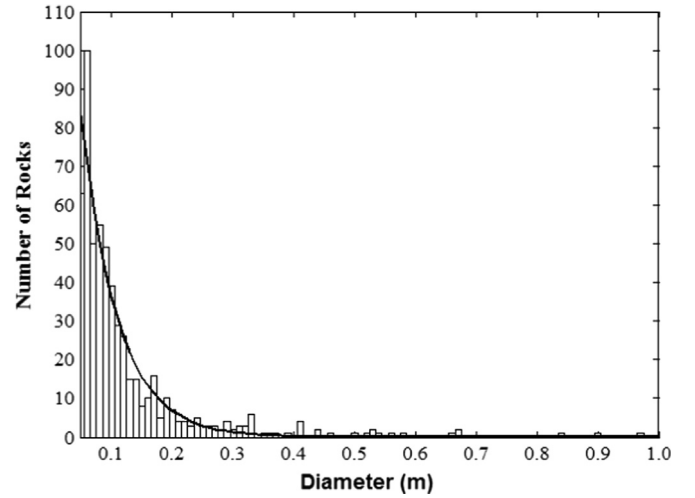


Fig. 7. Histogram showing the number of rocks of each diameter. Binned data and the power law function fit are shown.

The height-to-diameter (H/D) and height-to-maximum-diameter (H/D_{max}) ratios are important lunar rock parameters. Table 5 lists the statistical results from the Lunokhod-1 and 2 and Apollo 11–17 sites (Demidov and Basilevsky, 2014). Rocks at the CE-3 site have lower height-to-diameter ratios compared to rocks from other lunar missions, indicating that the rocks at the CE-3 site are relatively flat. No significant geographic variations were found in the resulting H/D and H/D_{max} parameters. The average H/D for all 582 rocks at the CE-3 landing site is 0.31 with a standard deviation of 0.203. The 95% confidence interval for the average H/D is 0.31 ± 0.013 . This is consistent with the early recommendations of Hutton (1969) and with the H/D of Mars rocks as being around 0.5 (Golombek and Rapp, 1997) and falls within the H/D range of 0.2–0.9 (Florensky et al., 1971).

Note that the constant in Eq. (7) was not considered, and only H/D was calculated. Therefore, the H/D ratio is slightly different from the parameter in Eq. (7), which was calculated as 0.234 in Section 4.4.

5. Discussion

The Yutu rover drove 114 m on the ejecta blanket of crater C1. There are many small, fresh impact craters in the landing area, and

Table 2
Rock number for each waypoint.

Site	Maximum diameter (m)	Minimum diameter (m)	Average diameter (m)	Maximum height (m)	Minimum height (m)	Average height (m)	Total number
N0101	1.533	0.050	0.146	0.359	0.001	0.034	198
N0102	0.668	0.053	0.164	0.314	0.001	0.040	81
N0103	0.841	0.051	0.147	0.129	0.002	0.040	50
N0104	0.660	0.052	0.153	0.115	0.004	0.044	40
N0105	0.322	0.050	0.100	0.083	0.001	0.030	65
N0106	0.294	0.050	0.089	0.099	0.002	0.029	76
N0107	0.412	0.050	0.102	0.089	0.003	0.030	72

Table 3
Parameters for each waypoint.

Site	N0101	N0102	N0103	N0104	N0105	N0106	N0107	All sites
Rock area (m ²)	8.346	2.336	1.398	1.180	0.697	0.635	0.830	15.422
<i>k</i>	0.03639	0.0116	0.00547	0.00507	0.00360	0.00633	0.00481	0.0125
<i>l</i>	-1.216	-2.163	-1.506	-2.398	-7.969	-7.563	-6.803	-1.743
<i>R</i> ²	0.9908	0.8995	0.9977	0.9545	0.9673	0.9713	0.9752	0.9965

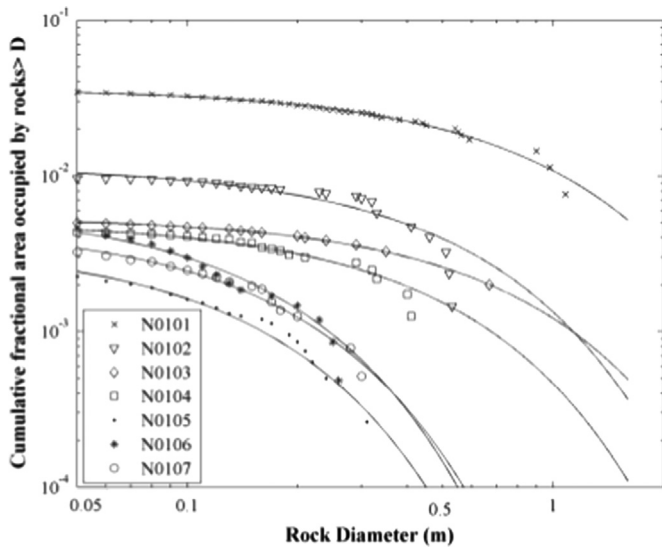


Fig. 8. Cumulative fractional area covered by rocks versus rock diameter at the CE-3 site.

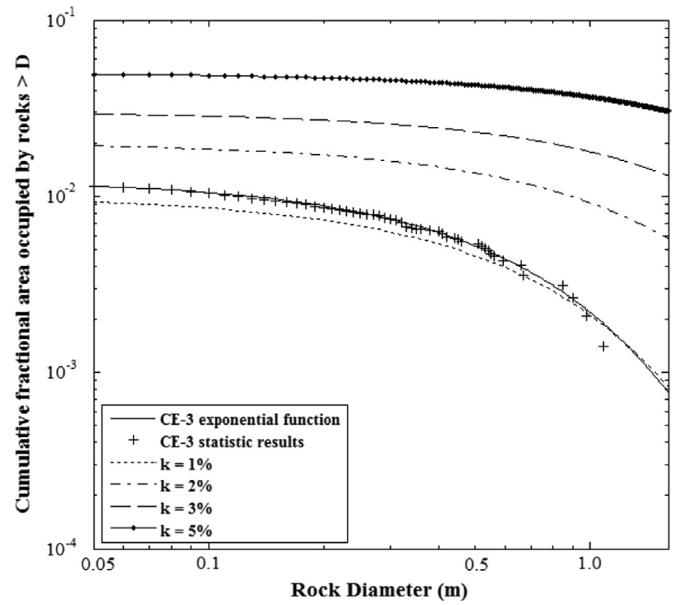


Fig. 9. Cumulative fractional area covered by rocks versus rock diameter at the CE-3 site. Exponential model size-frequency distributions from Eq. (2) for 1%, 2%, 3%, and 5% are also shown.

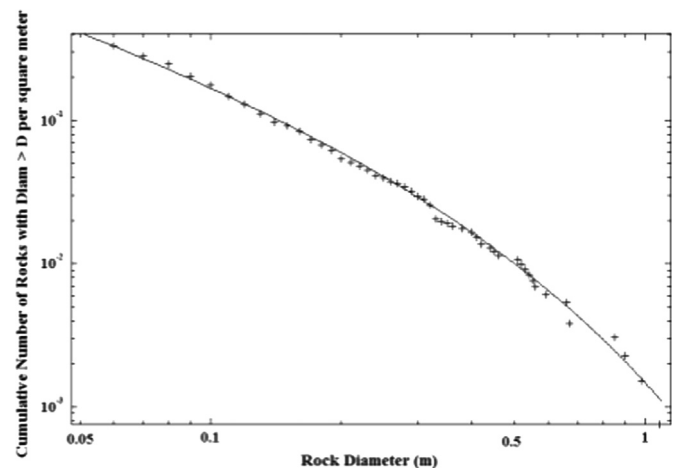


Fig. 10. Cumulative number of rocks per square meter greater than a given diameter versus rock diameter measured at the CE-3 site.

analyses of the relationship of size frequencies and space at the CE-3 landing site are valuable in investigating the mechanism of their formation.

A number of studies have been made on block distributions around craters on the lunar surface (Cintala and McBride, 1994; Hutton, 1969; Moore et al., 1969; Shoemaker and Morris, 1968; Bart and Melosh, 2007, 2010a, 2010b). Moore et al. (1969) found that the frequencies of rocks per unit area usually decrease with distance from a crater and, according to Surveyor statistics, frequencies of blocks around fresh lunar craters change with size, locale, and distance from the crater rim. The results show that frequencies of blocks larger than one meter across are higher on rough mare than on smooth mare. Shoemaker and Morris (1968) studied the size distribution of the fragmented debris in the strewn fields of blocks surrounding craters with raised rims at the Surveyor III landing site. Hutton (1969) showed that block distributions around craters vary from crater to crater. Cintala and McBride (1994) presented rock distributions for the Surveyor I, III, and VI sites as three distinct groups: blocks inside craters, blocks between craters, and all blocks. Moreover, complex relationships have been suggested to describe the decrease in both total rock abundance and maximum block size with distance from the crater

(Gaskell, 1993). According to Melosh (1989), the ejecta deposits of the smallest class of lunar craters (from 0.5 to about 1 km in diameter) that penetrate the fragmented regolith are blocky and show little structure.

The mare basalts at the landing site of CE-3 represent a type of unsampled lunar basalt and can be classified as medium-titanium basalts (Giguere et al., 2000). The Yutu rover surveyed a small area over the Eratosthenian basalts within the Imbrium basin. These mare basalts are believed to be among the youngest compared with the landing sites of the Apollo and Luna missions. As these lava flows are young, the regolith depth derived from high-frequency

LPR echoes varies from 2.2 m to 5.4 m with a median value of ~5 m (Zhang et al., 2015). This value is relatively thin when compared with the thickness of the regolith at the Apollo sites (which ranged from 3–4 m at the young Apollo 12 site up to over 6–8 m at the old Apollo 11 landing site). A consequence of a thin regolith is that, because the bedrock is close to the surface, small craters can excavate rocks from beneath the soil. This probably accounts for the rock distribution of the CE-3 landing site.

Compared to the 450 m diameter of crater C1, the distance (40 m) is much less than half of the radius, and the rock abundance beyond the radius cannot be determined. As crater C2 in Fig. 6b is blocky, it may have penetrated the regolith layer and excavated the underlying bedrock. When considered on a direct-count basis, the estimated rock distribution may have an apparent spatial relationship, being disposed more or less radially relative to crater C2. Table 6 lists rock areas designated as 0–R, R–2R, 2R–3R, 3R–4R, and 4R–5R around the C2 crater; statistics show that the rock abundance peaks at 2R–3R. The results proved to conform to the block distribution within 3R.

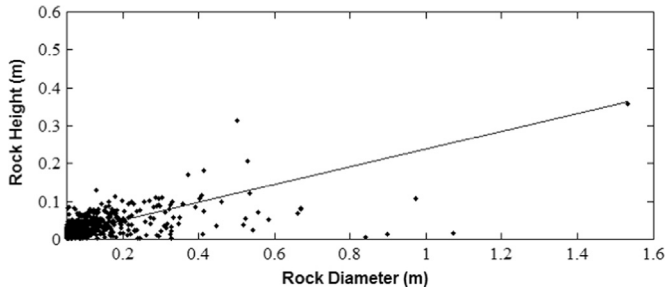


Fig. 11. Plot of rock height versus diameter. Data indicates that rock heights are 0.234 times their diameter, on average.

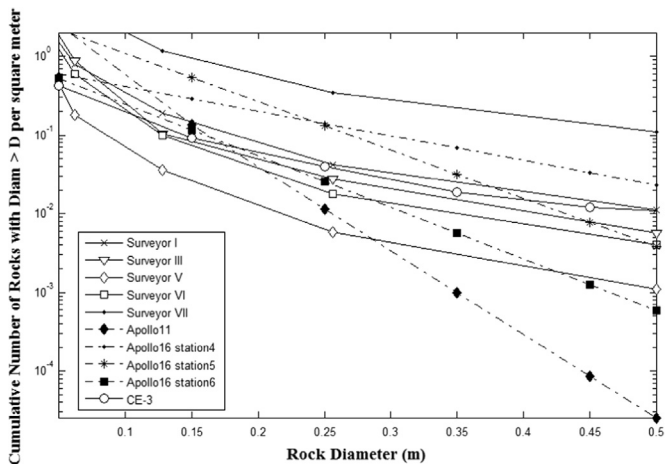


Fig. 12. Comparison of the cumulative number of rocks greater than a given diameter per square meter. Surveyor rock distributions are from Shoemaker and Morris (1968), the Apollo 11 rock distribution is from Aldrin et al. (1969), and Apollo 16 rock distributions are from Muehlberger et al. (1972).

6. Conclusions

Research on rock abundance and distribution is of great importance in determining lander and/or rover landing sites. Meanwhile, knowledge of the rock population may lead to a better understanding of geological site information. In this paper, the size-frequency distributions of rocks at the CE-3 lunar landing site were analyzed. Rock data were obtained from Navcam stereo images from 7 waypoints, covering most of the CE-3 traversal area. The plot of cumulative fractional area versus diameter fits well with an exponential function. These rock data display a convex-up curve shape on a log–log plot. The cumulative number of rocks of a certain diameter, obtained by numerically integrating the cumulative fractional area curve, shows that the curve fits well with the data. The plots of the cumulative number and cumulative area distributions had portions with distinct slopes. Comparison with Apollo, Surveyor, and Lunokhod lunar mission data show that the

Table 6
Rock areas around the C2 crater.

	0–R	R–2R	2R–3R	3R–4R	4R–5R
Rock area (m ²)	1.185	4.7951	5.3802	2.0118	0.9068
Fractional area	2.50%	2.67%	3.89%	0.89%	0.44%

Table 4

Cumulative number of rocks with diameters larger than 0.1 m (Shoemaker and Morris, 1968; Aldrin et al., 1969; Muehlberger et al., 1972).

Site*	A11	A16-4	A16-5	A16-6	CE-3	SI	SIII	SV	SVI	SVII
Cumulative number of rocks	0.47	0.41	1.10	0.24	0.17	0.34	0.30	0.07	0.20	1.97

* We have abbreviated Apollo as A, Surveyor as S, and Lunokhod as L in Tables 4 and 5.

Table 5

Values of the H/D and H/D_{max} parameters for Lunokhod-1 and 2 and Apollo 11–17 (Demidov and Basilevsky, 2014)*.

	L1	L2	A11	A12	A14	Ao15	A16	A17	CE-3
Number	108	116	45	34	38	34	35	35	5824
Average H/D	0.64	0.60	0.59	0.57	0.54	0.58	0.63	0.52	0.31
Average H/D_{max}	0.58	0.54	0.53	0.51	0.49	0.52	0.57	0.47	0.28

* We have abbreviated Apollo as A, Surveyor as S, and Lunokhod as L in Tables 4 and 5.

entire rock distribution curve at the CE-3 site is similar to that found in the Surveyor III mission.

Acknowledgments

This work was supported by the National Natural Science Foundation of China (Grant nos. 41201480, 41171355, 41471388, 41472303 and 41590851) and the Key Research Program of the Chinese Academy of Sciences (Grant no. KGZD-EW-603) and Open Research Fund of State Key Laboratory of Information Engineering in Surveying, Mapping and Remote Sensing of China (Grant no. 1402).

References

- Aldrin, E.E., Armstrong, N.A., Collins, M., 1969. Crew Observations. Apollo 11 Preliminary Science Report NASA SP-214. Published by NASA, Washington, D.C., pp. 42–47.
- Bauch, K.E., Hiesinger, H., Weinauer, J., Robinson, M.S., Scholten, F., 2013. Estimated Rock Abundances at the Apollo and Luna Landing Sites. In: Proceedings of the EGU General Assembly Conference Abstracts. Vol. 15, p. 8053.
- Bandfield, J.L., Ghent, R.R., Vasavada, A.R., Paige, D.A., Lawrence, S.J., Robinson, M.S., 2011. Lunar surface rock abundance and regolith fines temperatures derived from LRO Diviner Radiometer data. *J. Geophys. Res.* 116, E12.
- Basilevsky, A.T., Abdrakhimov, A.M., Head, J.W., Pieters, C.M., Wu, Y.Z., Xiao, L., 2015. Geologic characteristics of the Luna17/Lunokhod1 and Chang'E-3/Yutu landing sites, Northwest Mare Imbrium of the Moon. *Planet. SpaceSci.* 117, 385–400.
- Bart, G.D., Melosh, H.J., 2007. Using lunar boulders to distinguish primary from distant secondary impact craters. *Geophys. Res. Lett.* 34, L07203. <http://dx.doi.org/10.1029/2007GL029306>.
- Bart, G.D., Melosh, H.J., 2010a. Distributions of boulders ejected from lunar craters. *Icarus* 209, 337–357. <http://dx.doi.org/10.1016/j.icarus.2010.05.023>.
- Bart, G.D., Melosh, H.J., 2010b. Impact into lunar regolith inhibits high-velocity ejection of large blocks. *J. Geophys. Res.* 115, E08004. <http://dx.doi.org/10.1029/2009JE003441>.
- Bugliacchi, R., Guest, J.E., 2008. Compositional and temporal investigation of exposed lunar basalts in the Mare Imbrium region. *Icarus* 197, 1–18.
- Cameron, W.S., Coyle, G.J., 1971. An analysis of the distribution of boulders in the vicinity of small lunar crater. *Moon* 3, 159–188.
- Christensen, P.R., 1986. The spatial distribution of rocks on Mars. *Icarus* 68, 217–238.
- Cintala, M.J., McBride, K.M., 1994. Block distributions on the lunar surface: a comparison between measurements obtained from surface and orbital photography. In: Proceedings of the Lunar and Planetary Science Conference. Vol. 2, pp. 261–262.
- Demidov, N.E., Basilevsky, A.T., 2014. Height-to-diameter ratios of Moon rocks from analysis of Lunokhod-1 and -2 and Apollo 11–17 panoramas and LROC NAC images. *Sol. Syst. Res.* 48 (5), 324–329.
- Florensky, K.P., Basilevsky, A.T., Pronin, A.A., Popova, Z.V., 1971. Preliminary results of panoramas geomorphological research in Peredvizhnaya laboratoriya na Lune –Lunokhod-1 (Lunokhod-1: Movable Laboratory on the Moon). *Nauka, Moscow*, 96–115.
- Garvin, J.B., Mouginiis-Mark, P.J., Head, J.W., 1981. Characterization of rock populations on planetary surfaces: techniques and a preliminary analysis of mars and venus. *Moon Planet.* 24, 355–387.
- Gaskell, R., 1993. Martian surface simulations. *J. Geophys. Res.* 98, 11099–11103.
- Giguere, T.A., Taylor, G.J., Hawke, B., Lucey, P.G., 2000. The titanium contents of lunar mare basalts. *Meteorit. Planet. Sci.* 35, 193–200.
- Golombek, M.P., Rapp, D., 1997. Size-frequency distributions of rocks on Mars and Earth analog sites: implications for future landed missions. *J. Geophys. Res.* 102, 4117–4129.
- Golombek, M.P., Cook, R.A., Moore, H.J., Parker, T.J., 1997. Selection of the Mars Pathfinder landing site. *J. Geophys. Res.* 102, 3967–3968.
- Golombek, M.P., Moore, H.J., Haldemann, A.F.C., Parker, T.J., Schofield, J.T., 1999. Assessment of Mars Pathfinder landing site predictions. *J. Geophys. Res.* 104, 8585–8594.
- Golombek, M.P., Haldemann, A.F.C., Forsberg-Taylor, N.K., DiMaggio, E.N., Schroeder, R.D., Jakosky, B.M., Mellon, M.T., Matijevic, J.R., 2003. Rock size-frequency distributions on Mars and implications for Mars exploration rover landing safety and operations. *J. Geophys. Res.: Planet.* 108, E12.
- Golombek, M.P., Crumpler, L.S., Grant, J.A., Greeley, R., Cabrol, N.A., Parker, T.J., Rice Jr, J.W., Ward, J.G., Arvidson, R.E., Moersch, J.E., Ferguson, R.L., Christensen, P.R., Castaño, A., Castaño, R., Haldemann, A.F.C., Li, R., Bell III, J.F., Squyres, S.W., 2006. Geology of the Gusev cratered plains from the spirit rover transverse. *J. Geophys. Res.: Planet.* 111, E2.
- Golombek, M.P., Huertas, A., Marlow, J., McGrane, B., Klein, C., Martinez, M., Arvidson, R.E., Heet, T., Barry, L., Seelos, K., Adams, D., Li, W., Matijevic, J.R., Parker, T., Sizemore, H.G., Mellon, M., McEwen, A.S., Tamppari, L.K., Cheng, Y., 2008. Size-frequency distributions of rocks on the northern plains of Mars with special reference to Phoenix landing surfaces. *J. Geophys. Res.* 113, E00A09.
- Golombek, M.P., Huertas, A., Kipp, D., Calef, F., 2012a. Detection and characterization of rocks and rock size-frequency distributions at the final four Mars science laboratory landing sites. *Mars* 7, 1–22.
- Golombek, M.P., Grant, J., Kipp, D., Vasavada, A., Kirk, R., Ferguson, R., Bellutta, P., Calef, F., Larsen, K., Katayama, Y., Huertas, A., Beyer, R., Chen, A., Parker, T., Pollard, B., Lee, S., Sun, Y., Hoover, R., Sladek, H., Grotzinger, J., Welch, R., Noe Dobrea, E., Michalski, J., Watkins, M., 2012b. Selection of the Mars science laboratory landing site. *Space sci. rev.* 170 (1–4), 641–737.
- Grant, J.A., Wilson, S.A., Ruff, S.W., Golombek, M.P., Koestler, D.L., 2006. Distribution of rocks on the Gusev plains and on Husband hill, Mars. *Geophys. Res. Lett.* 33, L16202.
- Heet, T.L., Arvidson, R.E., Cull, S.C., Mellon, M.T., Seelos, K.D., 2009. Geomorphic and geologic settings of the Phoenix Lander mission landing site. *J. Geophys. Res.* 114, E00E04.
- Heiken, G.H., Vaniman, D.T., French, B.M., 1991. Lunar Sourcebook : A User's Guide to the Moon. Cambridge University Press, Cambridge, UK, p. 753, Research Supported by NASA.
- Hutton, R.E., 1969. Lunar surface models. NASA Technique report.
- Li, C., Mu, L., Zou, X., Liu, J., Ren, X., Zeng, X., Yang, Y., Zhang, Z., Liu, Y., Zuo, W., Li, H., 2014. Analysis of the geomorphology surrounding the Chang'e-3 landing site. *Res. Astron. Astrophys.* 14, 1514.
- Liu, Z., Di, K., Peng, M., Wan, W., Liu, B., Li, L., Yu, T., Wang, B., Zhou, J., Chen, H., 2015. High precision landing site mapping and rover localization for Chang'e-3 mission. *Sci China Phys. Mech. Astron.* 58 (1), 1–11.
- Melosh, H.J., 1989. Impact Cratering: A Geologic Process, (Oxford Monographs on Geology and Geophysics No. 11). Oxford University Press, New York, p. 253. (Research supported by NASA).
- Moore, H.J., Pike, R.J., Ulrich, G.E., 1969. Lunar Terrain and Traverse Data for Lunar Roving Vehicle Design Study, March 19: preliminary US Geological Survey Report.
- Moore, H.J., 1971. Large Blocks Around Lunar Craters. Analysis of Apollo 70 Photography and Visual Observations NASA SP-232. pp. 26–27.
- Muehlberger, W.R., Batson, R.M., Boudette, E.L., Duke, C.M., Eggleton, R.E., Elston, D. P., England, A.W., Freeman, V.L., Hait, M.H., Hall, T.A., Head, J.W., Hodges, C.A., Holt, H.E., Jackson, E.D., Jordan, J.A., Larson, K.B., Milton, D.J., Reed, V.S., Rennilson, J.J., Schaber, G.G., Schafer, J.P., Silver, L.T., Stuart-Alexander, D., Sutton, R.L., Swann, G.A., Tyner, R.L., Ulrich, G.E., Wilshire, H.G., Wolfe, E.W., Young, J.W., 1972. Preliminary Geologic Investigation of the Apollo 16 landing site, Apollo 16 Preliminary Science Report. Published by NASA, Washington, D. C., pp. 107–108.
- Ouyang, Z.Y., 2005. Introduction to Lunar Science. Chinese Aerospace Press, Beijing.
- Peng, M., Wan, W., Wu, K., Liu, Z., Li, L., Di, K., Li, L., Miao, Y., Zhan, L., 2014. Topographic mapping capability analysis of Chang'e-3 Navcam stereo images and three-dimensional terrain reconstruction for mission operation. *J. Remote Sens.* 18 (5), 995–1002.
- Qiao, L., Xiao, L., Zhao, J., Huang, Q., Haruyama, J., 2014. Geological Features and Evolution History of Sinus Iridum, the Moon. *Planet. Space Sci.* 101, 37–52.
- Shoemaker, E.M., Morris, E.C., 1968. Size-Frequency Distribution of Fragmental Debris, Jet Propulsion Laboratory, Surveyor Project Final Report, Part II. Science Results, pp. 86–136.
- Urquhart, M.L., Mellon, M.T., 2007. A new model for determining lunar rock abundance and landing hazards. In: Proceedings of the Lunar and Planetary Institute Science Conference Abstracts, p. 2171.
- Ward, J.G., Arvidson, R.E., Golombek, M., 2005. The size-frequency and areal distribution of rock clasts at the spirit landing site, Gusev crater, Mars. *Geophys. Res. Lett.* 32, L11203.
- Wilhelms, D.E., McCauley, J.F., 1971. Geologic Map of the Near Side of the Moon. US Geological Survey Miscellaneous Geological Investigations Map I-703, Denver.
- Wu, B., Li, F., Ye, L., Qiao, S., Huang, J., Wu, X., Zhang, H., 2014. Topographic modeling and analysis of the landing site of Chang'E-3 on the Moon. *Earth Planet. Sci. Lett.* 405, 257–273.
- Xiao, L., 2014. China's touch on the Moon. *Nat. Geosci.* 7, 391–392.
- Xiao, L., Zhu, P., Fang, G., Xiao, Z., Zou, Y., Zhao, J., Zhao, N., Yuan, Y., Qiao, L., Zhang, X., Zhang, H., Wang, J., Huang, J., Huang, Q., He, Q., Zhou, B., Ji, Y., Zhang, Q., Shen, S., Li, Y., Gao, Y., 2015. A young multilayered terrane of the northern Mare Imbrium revealed by Chang'E-3 mission. *Science* 347 (6227), 1226–1229.
- Yingst, R.A., Haldemann, A.F.C., Biedermann, K.L., Monhead, A.M., 2007. Quantitative morphology of rocks at the Mars Pathfinder landing site. *J. Geophys. Res.* 112, E06002.
- Zhao, J., Huang, J., Qiao, L., Xiao, Z., Huang, Q., Wang, J., Xiao, L., 2014. Geologic characteristics of the Chang'E-3 exploration region. *Sci. China Phys. Mech. Astron.* 57 (3), 569–576.
- Zhang, J., Yang, W., Hu, S., Lin, Y., Fang, G., Li, C., Peng, W., Zhu, S., He, Z., Zhou, B., Lin, H., Yang, J., Liu, E., Xu, Y., Wang, J., Yao, Z., Zou, Y., Yan, J., Ouyang, Z., 2015. Volcanic history of the Imbrium basin: a close-up view from the lunar rover Yutu. *PNAS* 112 (17), 5343–5347.